A Contactless Approach to Monitor Rail Vibrations

A Contactless Approach to Monitor Rail Vibrations

Cite this article as: A. Enshaeian, L. Luan, M. Belding, H. Sun, P. Rizzo, A Contactless Approach to Monitor Rail Vibrations, Experimental Mechanics https://doi.org/10.1007/s11340-021-00691-z

A Contactless Approach to Monitor Rail Vibrations

A. Enshaeian[1], L. Luan[2], M. Belding[1], H. Sun[2,3], P. Rizzo[1*]

[1]Laboratory for Nondestructive Evaluation and Structural Health Monitoring Studies, Department of Civil and Environmental Engineering, University of Pittsburgh, Pittsburgh, PA 15261, USA

[2]Department of Civil and Environmental Engineering, Northeastern University, Boston, MA 02115, USA

[3]Department of Civil and Environmental Engineering, MIT, Cambridge, MA 02139, USA

[*]Corresponding author email: pir3@pitt.edu

ABSTRACT

Background

Continuous welded rails (CWR) are subjected to thermal effects that may lead to buckling or fracture during warm or cold seasons, respectively. The modal characteristics (frequency and mode shapes) of CWR may reveal important information about the thermal stress that can be used to prevent rail failures.

Objective

The primary objective of this study is to prove a contactless method to monitor the vibration and to extract the modal characteristics of rails using a high-speed camera and advanced image processing. This study is the first step towards a general noninvasive monitoring paradigm aimed at measuring axial stress in CWR. **Methods**

To prove the principles of the proposed paradigm, a finite element model of an unrestrained rail segment under varying length, boundary conditions, and axial stresses was formulated. The results of the model were then used to interpret the experimental results relative to a 2.4 m-long rail subjected to compressive loading-unloading cycles. During the experiment, the rail was subjected to the impact of an instrumented hammer and the triggered vibration was recorded with a high-speed camera. The videos were then processed using the phase-based displacement extraction, motion magnification, as well as dynamic mode decomposition techniques to extract the modal characteristics of the specimen.

Results

The results show that the frequencies extracted from the images matched well those obtained with two conventional accelerometers bonded to the rail while the mode shapes extracted from the videos matched those predicted numerically. Additionally, the numerical analysis enabled the interpretation of some unexpected experimental results.

Conclusions

The results presented here proved that the proposed method to infer axial stress in CWR requires proper modeling in order to link the modal characteristics of the rails to the axial stress. In the future, the finite element formulation presented here will be expanded to model CWR under given cross-ties and fasteners conditions in order to link the modal characteristics of the rail of interest to its axial stress.

Keywords: continuous welded rails, finite element analysis, image processing, rail neutral temperature

Introduction

At time of installation, continuous welded rail (CWR) are pre-tensioned to compensate the thermal expansion occurring in warm days. The typical pre-tension is such that the temperature T_N at which the net longitudinal force is zero, typically referred to as the rail neutral temperature (RNT), is between 32°C and 43°C [1]. Values above 43°C increase the risk of rail fracture during the cold season whereas neutral temperature lower than 32°C increases the risk of thermal buckling during the warm season. Unfortunately, any given rail is "physiologically" subjected to decrease in neutral temperature due to operational conditions and maintenance. The amount of decrease is typically unknown increasing the uncertainties relative to the risk of extreme compression in hot days.

Axial stress and neutral temperature are typically linked by considering a CWR structurally equivalent to an ideal column. Under this assumption, buckling is expected to occur when the temperature T_R of the rail steel reaches the critical temperature T_{cr}, using the formula:

$$\frac{\sigma_{cr}}{E\alpha} + T_N = T_{cr} \qquad (1)$$

In Eq. (1), σ_{cr} is the critical stress of the rail, and E and α indicate the Young's modulus and the coefficient of thermal expansion of the steel, respectively. As the values of σ_{cr}, E, and α are typically known by design, buckling may be predicted and therefore prevented by estimating the critical temperature T_{cr} at which the rail buckles. Equation (1) requires the knowledge of T_N. This can be attained by measuring the longitudinal stress σ_R at any temperature T_R and then infer T_N using the equation:

$$T_N = T_R - \frac{\sigma_R}{E\alpha} \qquad (2)$$

where σ_R is considered positive when the rail is in compression.

Based on the above there is a need for cost-effective noninvasive methods to measure the RNT *in situ*. Current methods are based on statics or dynamic principles and may rely on acoustics, ultrasounds, or electromagnetism. The beam-column bending theory is the foundation of the Vertical Rail Stressing Equipment (VERSE®) [2], perhaps the most popular commercial system currently in use. This static method links the axial load acting on the rail to the vertical force required to lift the same rail by a certain amount. By the axial load to the cross-sectional area of the rail, the stress $?_R$ is determined and then used in Eq. (2) to estimate the neutral temperature. This test can be performed only when the track is in tension, i.e. the rail temperature must be lower than the true, but usually unknown, RNT. In addition, about 30 meters of rail must be unanchored from the fasteners, a support spacer is placed 10 meters away from the mid-span. Another commercial system consists of strain gages welded to the web of the rail of interest to quantify the rate of decay of the neutral temperature [3]. The longitudinal strain data collected by the gages are transmitted wirelessly to collector units mounted on wayside towers. To be effective, the system must remain in place for months if not years. The Magnetic Barkhausen Noise (MBN) measures the variations of the rail's magnetic permeability due to the stress. Tension leads to an increase of the permeability and vice versa. MBN provides a quantitative evaluation of the permeability, and therefore an indirect assessment of the rail's stress [4]. The method requires calibration, performed in laboratory using calibration rails, and the data may be adversely affected by residual stresses, unevenness, rust, and paint coating on the rail [3].

Other methods have not been translated yet into commercial systems. For example, the electromechanical impedance technique exploits the relationship between the electrical impedance of a piezoelectric transducer (PZT) and the mechanical impedance of the host structure to which the PZT is bonded [5, 6]. In order to capture the zero stress, the RNT needs to be crossed. This is possible under favorable weather (cool-warm-cool temperature) and hours of testing. The ultrasonic birefringence method uses linearly polarized shear waves propagating along two perpendicular directions. The difference in the time-of-flight of these two beams depends upon the stress and the residual stress on the material [7]. The approach requires extremely accurate measurements, attainable only with expensive equipment. An interesting approach consists of transmitting and receiving nonlinear ultrasonic guided waves along rail webs [8-11]. A nonlinear parameter associated with the higher order harmonics was found to be stress-dependent. As for the EMI, this method requires multiple measurements over a day period during which the RNT must be crossed.

In recent years, Rizzo and co-authors investigated the interaction between highly nonlinear solitary waves propagating along monodisperse chain of uniform spherical particles and axially stressed beams in point contact with the chain [12-16]. The method was successfully proven onto two rail segments under laboratory conditions [16] but was not tested in real tracks.

In the study presented in this paper, an approach based on structural dynamics and non-contact vibration monitoring using cameras operating at frame rates higher than conventional 30 Hz was considered. The overall research hypothesis is that the modal characteristics (frequency and mode shapes) depend upon the longitudinal stress at any given rail geometry and boundary conditions, which include cross-ties, ballast, and fasteners. With the use of proper finite element analysis (FEA) such interdependency among stress, modal characteristics, and boundary conditions can be established. In the field, the pixels of videos recorded with a high-speed camera can be considered as virtual accelerometers to extract the frequencies and the mode shapes that are then linked to the axial stress using the numerical predictions of the FEA. The proposed approach aligns with some recent researches where high-speed cameras were proposed to replace traditional physical contact sensors like accelerometers or expensive contactless instruments such as laser vibrometers for the non-contact measurement of modal characteristics for structural health monitoring (SHM) applications. This emerging noncontact vision-based technique is eased by the widespread diffusion of affordable high-speed consumer-grade video cameras, and by the rapid development of image processing algorithms [17-19]. Many of these approaches are based on tracking techniques which requires notable features like markers for tracking on the surface of the structures. Furthermore, the tracking approach fails when the motion is very small like sub-pixel level movement. To deal with these problems, new video processing techniques, phase-based displacement extraction [20] combined with motion magnification [21], were proposed to measure the small subpixel displacement as well as to identify the mode shapes. The phased-based technique for modal identification was initially demonstrated with the vibration of a cantilever beam in the lab [20]. Then, these approaches were applied to civil infrastructures like antenna tower and bridge [22, 23], or to identify the dynamics of a real-world wind turbine blade [24].

In the study presented in this article, a 2.4 m. long AREMA rail was mounted on an MTS machine and subjected to compressive load up to 40% of its critical load (under the assumption of pin-pin boundary conditions). At discrete load steps, the side of the rail head was hit with an instrumented hammer to trigger vibration along the weak axis of inertia. The vibrations were monitored with a high-speed high-

resolution camera and the corresponding frequencies and mode-shapes were extracted with a motion magnification algorithm. The frequencies were compared with those extracted from the Fourier transforms associated with two conventional accelerometers bonded to the rail. To generalize the study, interpret the experimental results, and emphasize how the proposed approach can be applied in the field, a FEA of an unfastened rail of different lengths, boundary conditions, and longitudinal stresses was conducted to predict the frequency of vibration and the corresponding mode-shapes of the first few lateral, transverse, and torsional modes.

The main scientific novelty of the paper is the combination of classic FEA and advanced imaging processing to extract the modal characteristics of CWR. Besides the preliminary work involving thin and thick beams [25], this is the first study in which a video-based SHM method is applied to a rail under laboratory conditions. The outcome of the study presented in this article is the first milestone of a long-term aim to develop a reliable contactless method for the noninvasive measurement of axial stress, and ultimately neutral temperature. This contactless method would rely in the finite element model of the rail of interests to associate the modal characteristics of the rail extracted from the videos to the longitudinal stress $?_R$, at given boundary conditions and geometries.

The paper is structured as follows. Section 2 provides a brief background about the image processing algorithm. Section 3 describes the finite element model implemented in ANSYS. Section 4 presents the experimental setup along with the numerical and experimental results. Finally, Section 5 ends the article with some concluding remark and suggestions for possible future studies.

Image Processing Algorithm

In this study, the recorded test videos were analyzed with a phase-based motion extraction technique to obtain the vibration frequency and visualize the mode shapes. As the motion of rail vibration is very small (subpixel level), traditional tracking approach fails to get the displacement. Here the phase-based displacement extraction method [20] was employed to obtain the subpixel displacements followed by the frequency spectrum. After getting the frequency peaks, the motion magnification [21] was applied to visualize the mode shapes within the given specified frequency bands.

Phase-based Displacement Extraction

In the phase-based displacement extraction method [20], all the frames of the original video are manipulated with quadrature complex filters which leads to local phase and amplitude. The spatial local phase and local amplitude are quantities analogous to the phase and amplitude of Fourier series coefficients. The phase controls the location of basis function while the amplitude controls its strength. In the case of the Fourier transform, the phase corresponds to global motion. The local phase gives a way to compute the local motion. For a video, with image brightness specified by $I(x,y,t)$ at spatial location (x,y) and time t, the local phase and local amplitude in orientation θ at a frame at time t_0 are computed by spatially bandpassing the frame with a complex filter $G_2^\theta + iH_2^\theta$ to get:

$$A_\theta(x,y,t_0)e^{i\phi_\theta(x,y,t_0)} = (G_2^\theta + iH_2^\theta) \otimes I(x,y,t_0) \qquad (3)$$

where $A_\theta(x,y,t_0)$ is the local amplitude and $\phi_\theta(x,y,t_0)$ is the local phase. The filters G_2^θ and H_2^θ are convolution kernels for processing the video frame and represent a quadrature pair that differs in phase by 90°. Figure 1 shows the filters used to compute local phase and local amplitude. These images represent a 9 by 9 grid of numbers where the gray level corresponds to the value of the filter [20].

Research has shown that constant contours of the local phase through time correspond to the displacement signal. The displacement signal can be obtained from the motion of constant contour of local phase in time. This can be expressed as:

$$\phi_\theta(x,y,t) = c \qquad (4)$$

for some constant c.

The displacement signal in a single direction then comes from the distance that the local phase contours move between the first frame and the current frame. Differentiating with respect to time yields

$$\left[\frac{\partial\phi_\theta(x,y,t)}{\partial x}, \frac{\partial\phi_\theta(x,y,t)}{\partial y}, \frac{\partial\phi_\theta(x,y,t)}{\partial t}\right] \cdot (u,v,1) = 0 \qquad (5)$$

where u and v are the velocity in the x and y directions respectively. It is noted that $\partial\phi_0(x,y,t)/\partial y \approx 0$ and $\partial\phi_{\pi/2}(x,y,t)/\partial x \approx 0$. The velocities in units of pixel can then be obtained:

$$u = -\left[\frac{\partial\phi_0(x,y,t)}{\partial x}\right]^{-1}\frac{\partial\phi_0(x,y,t)}{\partial t} \qquad (6)$$

and

$$v = -\left[\frac{\partial \phi_{\pi/2}(x,y,t)}{\partial y}\right]^{-1}\frac{\partial \phi_{\pi/2}(x,y,t)}{\partial t} \qquad (7)$$

To extract horizontal and vertical displacement d_x and d_y at a given time t_0, both sides of Eqs. (6) and (7) are integrated, namely,

$$d_x(t_0) = -\left[\frac{\partial \phi_0(x,y,t_0)}{\partial x}\right]^{-1}[\phi_0(x,y,t_0) - \phi_0(x,y,0)] \qquad (8)$$

and

$$d_y(t_0) = -\left[\frac{\partial \phi_{\pi/2}(x,y,t_0)}{\partial y}\right]^{-1}[\phi_{\pi/2}(x,y,t_0) - \phi_{\pi/2}(x,y,0)] \qquad (9)$$

From Equations (8) and (9), the pixel motion of each frame in the video is obtained.

Phase-based Motion Magnification

Motion magnification is an algorithm to magnify the motion of a video. The algorithm was initially proposed by Wu et al. [26] who built an Eulerian video magnification framework. Since this framework supports only small magnification factors at high spatial frequencies and can significantly amplify noise when the magnification factor is increased, Wadhwa et al. [21] proposed the phase-based motion magnification technique. The workflow of the phase-based motion magnification technique is as follows. The original video is firstly decomposed into the local spatial amplitude and phase using a complex-valued steerable pyramid filter bank [27]. The local phase signals are temporally band-passed to isolate specific temporal frequencies relevant to a given application and remove any temporal DC component which represent the motions in different scales and orientations. Then, the bandpassed phases are multiplied by an amplification factor which determines the magnification of the motion. Finally, the phase signals are combined back to from a video which has magnified motion in a specified band of temporal frequencies. For mode shape identification, the video within the frequency band near to the frequency peak is magnified to visualize the mode shapes. More details about this approach can be found in [20, 21]. We employed this approach to identify the full-field mode shapes from test videos. In addition, given the extracted full-field motion field, the dynamic mode decomposition (DMD) is employed to identify the

mode shapes and their corresponding source signals for different vibration frequencies. DMD seeks a best-fit linear operation for the discrete-time dynamical system and the linear operation can be treated as the finite-dimensional approximation of the Koopman operator. DMD computes the leading eigendecomposition of this operator, which results in the eigenvectors called DMD modes or dynamic modes and their corresponding eigenvalues [28, 29]. The following experimental analysis shows the efficacy of DMD for identification of the motion shapes and source signals for different vibration frequencies.

Finite Element Model of the Rail

Setup

Several models exist to describe the buckling of thermally stressed CWR. These models can be clustered at large in two groups. In the first group, the railroad track is replaced by an "equivalent" single beam of finite length that is examined using analytical or finite element models [30-32]. In the second group, CWR are considered equivalent to two parallel beams of finite length connected by linear springs located at the nodes of finite element mesh. The springs account for the lateral resistance provided by the ballast and the cross-ties [33-36]. For both single and double beam models, the ends of the "equivalent" beam(s) were considered as fixed supports.

In the study presented here, the first approach was adopted because real buckling typically begins from one track and then propagates to the second track through the crossties. In addition, the experimental validation involved a single rail segment. A straight rail with no imperfection and lengths comprised between 0.5 and 4 m at 0.25 m steps was modeled. The model did not include much longer rails (10 to 20 m) because the temperature change (with respect to the neutral temperature) at which the rail is expected to buckle would result much lower than the true T_{cr} typically observed in the field, as the lateral resistance provided by the cross-ties and the ballast is not taken into account properly. Rails shorter than 0.5 m were also ignored because too stiff: the corresponding buckling stress would result larger than the yield stress. It is noted here that the track buckle amplitude are typically in the order of 0.15 m to 0.75 m while its wavelength can be on the order of 12.2 – 24.4 m.

An AREMA 132 rail was modeled using ANSYS software, and BEAM188 and COMBIN14 elements. The latter are combined spring-damper elements and were used to take into account the lateral, flexural and torsional stiffness at the two ends. For the material, the properties of conventional ductile carbon steel

were used: Young's modulus of elasticity of 200 GPa, Poisson's ratio of 0.27 and density of 7930 kg/m^3. The finite element mesh was chosen based upon the mode shapes associated with the first two lateral, transverse, and torsional modes, and the ability to capture the mode shapes accurately. To verify the accuracy of the selected mesh, a few convergence analyses were conducted and it was determined that 40 beam elements were sufficient to model the single rail and no mesh refinement was necessary.

Each end of the rail was subjected to varying boundary conditions, modeled with three rotational springs according to the scheme presented in Fig. 2. Two rotational springs, hereinafter labeled as k_z and k_x, restrain the bending deflections with respect to the two principal axis of inertia. Following the notation of Fig. 2, these deflections identify the vibrations along the transverse (z-axis) and the lateral direction (x-axis) of the rail. The value of k_z ranged from pin-pin (close to zero) to fixed-fixed (i.e. infinitely rigid) supports; the same range was considered for the end supports k_x. The third rotational spring k_y was associated with torsion in order to model possible restraints to moment along the *y-axis* (resistance to torsion). A few different torsional stiffness k_y were considered. The boundary condition parameters for a real CWR is highly dependent on the fasteners and the ballast resistance. The stiffness associated with the fasteners and the ballast are not fixed numbers and may change from one location to another. Therefore, in order to model the effect of these supporting components in its best possible way, numerous spring coefficients are included in the numeric analyses to resemble the uncertainty of realistic rigidity at both ends.

Finally, several different axial forces on the rail were considered yielding to a total of 28,305 case scenarios run in ANSYS. Table 1 summarizes the variables considered and the number of steps between the minimum and maximum value for each variable. Specifically, 15 different rail lengths ranging from 0.5 meters up to 4 meter with 0.25-meter increments were considered. Thirty-seven axial loads were selected, spanning from 70% of pinned-pinned buckling compressive load, i.e. $0.7\frac{\pi^2 EI}{L^2}$, up to 20% tensile load, with an increment of 2.5% of the buckling load. Additionally, 17 different values for flexural bending spring coefficients and 3 torsional spring constants were included. The considered boundary coefficients cover the range from very low rigidity up to high stiffness for both the flexural and torsional springs. Consequently, any semi-rigid or realistic boundaries will lay inside this range. Regarding the flexural boundaries, the considered spring coefficients are between 0 up to 60 EI/L and for the torsional boundaries, this range is from 10 up to 100 GJ/L. Zero torsional stiffness at the two edges would lead to

instability of the beam along the torsional degree of freedom, thus the lowest coefficient is higher than zero. These sets of parameters resulted in 15x37x17x3=28,305 cases were simulated in ANSYS.

Numerical Results

To be able to compare the numerical predictions with the experimental results, this section presents the results associated with the rail vibrations with respect to the weak axis. Figure 3 displays a few mode-shapes associated with the following geometric and boundary conditions: torsional degree of freedom θ_y close to infinite, i.e. fully restrained, and θ_x and θ_z equal to $1.8\ EI_{min}/L$ and $1.8\ EI_{max}/L$, respectively. Figure 3a shows the lowest flexural deformation along the weak axis of inertia, which corresponds to the lowest frequency of vibration (43.61 Hz). Not shown here, the second lowest frequency of vibration is associated with the first transverse mode, i.e. the mode associated with the deflection across the strong axis of inertia. Figure 3b presents the 2nd lateral mode coupled to torsional deformations. The coupling is caused by the geometry of the cross-section in which the centroid and the shear center are not coincident. The consequence is that lateral bending stress induces torsion with respect to the shear center. Some studies have discussed this coupling mechanism [37, 38], noting that even for mode shapes with dominant lateral deformations, torsional angle response along the longitudinal direction of the beam is never zero. On the other hand, for torsional dominant modes, the rotation along the shear center induces some lateral deflections in the centroid. Finally Fig. 3c shows a pure torsional mode vibrating at 159.5 Hz.

With the dynamic responses of the rail such as those shown in Fig. 3, a set of numerical data were created in which the natural frequency of vibration for the first five lowest modes were predicted for various rail length, boundary conditions, and axial load. For illustrative purposes, a subset of these predictions is presented in Fig. 4, which shows the frequency as a function of the axial load for a 2.4 m long AREMA 132 rail with torsional springs infinitely rigid. Figure 4a refers to the pinned-pinned case, whereas Fig. 4b shows the results associated with the fixed-fixed boundary conditions. With the exception of the torsional modes, the frequencies decrease with the increase in compression. This is well-known in structural dynamics: in Fig. 4a (pinned-pinned rail), the load at which the first lateral frequency approaches zero represents the critical Euler buckling load. When the rail become stiffer because of the fixed-fixed ends, the frequencies in Fig. 4b are higher than those in Fig. 4a. Both figures also reveal that the torsional modes are largely unaffected by the load and the boundary conditions. These observations have important consequences when certain frequencies are to be used to estimate the axial stress. As a

matter of fact, different mode shapes exhibit different sensitivity to the axial load, In addition, the boundary conditions affect the sensitivity with respect to longitudinal stress. For example, based on what visible in Fig. 4a the first lateral mode of the pinned-pinned beam has a sensitivity of 8.3 Hz/MN. However for the fixed-fixed case shown in Fig. 4b the first lateral mode has a sensitivity of 4.9 Hz/MN. Changing the boundary condition also affects other modes, such that the sensitivity of the first transverse mode decreases from 3.6Hz/MN for the pinned-pinned case to 2.0 Hz/MN for the fixed-fixed condition. The order (from the lowest to higher frequencies at a given load) in which the modes exists depends on the boundary conditions of the rail, it is important between calculated mode shapes. For example, a pinned-pinned rail with infinite torsional stiffness (Fig. 4a), the first torsional mode would be observed after the first lateral, the first transverse and the first lateral-torsional mode. However, for a fixed-fixed rail with infinite torsional stiffness (Fig. 4b), the same torsional mode would be observed after the first lateral one. This phenomenon emphasizes the importance of estimating the boundary conditions in a rail and the importance of being able to identify the mode-shapes, as the estimation of the frequency only is not sufficient at labeling properly the nature of the vibration.

Model Validation

Experimental Setup

Figure 5 shows the overall experimental setup. The 2.4 m long rail was secured to an MTS machine. Mechanical compression at 100.7 kN step was applied up to 805.3 kN, and recorded with the MTS control box. The highest force corresponded to about 40% of the Euler buckling load under the assumption that the end boundary conditions were pinned-pinned. At each step, five vibrations were induced by impacting one side of the rail head with a heavy duty instrumented hammer (PCB Impulse Force Hammer, Model 086D20).

The vibrations were recorded with a Phantom MIRO C210 camera operating at 1,000 fps and 1280 x 1024 resolution, located 5.33 m from the rail in order to capture the motion of the whole rail. The setup was completed by two strain-gages mounted on the web of the rail and two accelerometers (located at L/4 from bottom and L/3 from top). The strain gages were used as a backup of the MTS readings and to detect any static bending along the weak axis of inertia during the experiment. The data from the accelerometers were sampled at 10 kHz and used to validate the results associated with the image processing.

Figure 6 shows the applied stress recorded with the MTS and with the strain gages. For the latter, the average of the readings from the two gages was determined. The figure demonstrates the repeatability of the loading and unloading ramps. Not shown here, the individual readings from each gage were similar implying the absence of any significant bending effects during the experiment.

Experimental Results (Acceleration Data)

For illustrative purposes, one time series measured from the accelerometer located at L/4 from bottom along the lateral direction is presented in Fig. 7a and the corresponding Fourier transform is presented in Fig. 7b overlapped with the spectrum of the transverse acceleration. Two clear peaks are visible at 48 Hz and 151 Hz. The latter was also captured along the transverse direction leading to the conclusion that these two peaks refer to the first lateral bending mode (48 Hz) and the first coupled lateral-torsional mode (151 Hz), respectively. This conclusion was confirmed by the finite element model in which the same rail was subjected to a forced function at its mid-span and by the image processing data presented later in this paper. As the mid-span of the rail head was impacted laterally by a hammer, the dominance of the first lateral mode is expected.

From the Fourier transform such as the one shown in Fig. 7b, the value of the frequency peaks at each level of load was extracted and charted against the applied load. The results relative to the accelerometer located at L/3 are summarized in Fig. 8 and are overlapped to the numerical predictions obtained for the same rail under pin-pin and fixed-fixed flexural boundary conditions, while fully restrained against torsion at both ends. Each dot represents the average frequency associated with the five impacts at a given load. The graph shows that as compression increased, the frequency did not decrease as expected. This behavior is attributable to the change in the boundary conditions: with the increase in compression, the rail became stiffer and cannot be still assumed pinned-pinned. Additionally, the assumption that the rail was infinitely rigid against torsion was too conservative.

Similar experimental findings were discussed in [39-41]. Livingston et al. [39] reported a mismatch in the calculated frequencies during loading and unloading cycles during a tension load test and attributed the difference to a change in the boundary conditions. Kish and Samavedam [40] provided temperature-dependent values for the pad-fastener system stiffnesses that could described the alterations in the boundary conditions within a tie-to-tie segment. However, Bayon et al. [41] observed a very similar phenomenon as depicted in Fig. 8 for a cylindrical component under compressive axial loads. Their

results showed that for low compressions “the cylinder behaves similarly to a sliding-sliding cylinder” while “the cylinder vibrates as a clamped–clamped one” under high compressions [41]. Therefore, it can be concluded that any vibration-based monitoring system aimed at estimating the axial stress requires a good estimation of the boundary conditions.

Experimental Results (Video Data)

The videos from the MIRO C210 camera were processed using the phase-based approach described in Section 2. At first, the time-history displacements of some pixels were investigated. In the phase-based displacement extraction method, only the pixels with sufficient contrast have measurable displacements. In testing the rail, the edges (i.e. the boundary between the rail and the background, and the boundary between the “qr-code” and the rail) had better contrast and deemed more reliable at measuring the lateral displacements. In order to alleviate the effect of measurement noise, displacements for all pixels with sufficient contrast were firstly extracted. To determine the pixels that had sufficient contrast, a minimum threshold on the amplitude coefficient which corresponds to the contrast was chosen. The threshold value used in this study was half of the median of the 20 pixels with the largest amplitude. Here, the displacements at the middle QR code (near the impact point) and the bottom “QR” code (Fig. 9) were extracted as an example with the extracted displacement time histories of these two points shown in Fig. 10. Note that the peak response shown in Fig. 10(b) indicates the impact event.

The displacement data were transformed into the frequency domain using fast Fourier transform (FFT). Then the frequency spectrum is obtained by averaging the FFT transform of all obtained pixel displacements at a given level of load. The result is presented in Fig. 11. Since each video consists of 2051 frames at 1,000 fps, the resolution of the frequency spectrum is too low (about 0.5 Hz). In this study, zero padding was applied to increase the frequency resolution of the spectra. Three peaks are visible in Fig. 11a. Nevertheless, the numerical analysis and the experimental result obtained from the acceleration measurements suggest that the peak around 120 Hz is a “false positive” mode. This was likely due to the flickering of the artificial light used to illuminate the rail. The hypothesis is confirmed by the spectrum shown in Fig. 11b, which is the Fourier transform of the time waveform associated with a control video recorded without hammer impact.

In order to identify the modes associated with the frequency peaks shown in Fig. 11a, the motion magnification technique was applied. The technique allows to “visualize” the mode shapes. Fig. 12 shows

two snapshots of the magnified video for the frequencies of 44.0 Hz and 149.9 Hz, respectively. The frequency bands for motion magnification are (1) 42 Hz - 46 Hz for the first mode with the amplification factor of 100, and (2) 148 Hz -152 Hz for the second mode with the amplification factor of 300. The magnified filtered videos show lateral and coupled lateral-torsional modes as shown in Fig. 12. To further verify the vibration modes, DMD was employed to identify the mode shapes and separate their corresponding source signals. Figs. 13 and 14 respectively show the mode shapes and source signals for the three frequency peaks shown in Fig. 11. It is shown that DMD decouples the mode shapes and source signals for different vibration frequencies. In Fig. 13a, the same vibration direction of all pixels along the rail and larger magnitude near the impact point demonstrate the first lateral mode. While the opposite vibration direction and inequal magnitude of the pixel at the same height along the rail indicates the torsion mode in Fig. 13c. The fake frequency peak does not show a clear vibration mode in Fig. 14b. It should be noted that the obtained mode shapes from DMD coincides with the visualized vibration shapes from the motion magnification as shown in Fig. 12.

To emphasize the ability to extract the modal characteristics of the rail with the use of the camera, Fig. 15 plots the value of the two frequency peaks as determined by the two accelerometers and by the camera. Figure 15a refers to the lowest flexural mode whereas Fig. 15b refers to the coupled mode. The experimental data are linearly interpolated. Both plots unequivocally demonstrate the excellent match between the contact approach and the contactless approach. If perfect match existed, the slope of the interpolation would be equal to 1.

Conclusions

In this paper, we presented a non-contact video-based monitoring system to extract the modal characteristics of rails. A laboratory experiment was conducted by testing a 2.4 m long rail subjected to loading-unloading compressive force and set to motion with an instrumented heavy-duty hammer. The images of the vibration were recorded with a high-resolution high-speed camera and processed with a motion magnification algorithm to identify the modes of vibration and the corresponding time-series displacement, which in turn were used to extract the frequencies of vibration. The experimental modal characteristics were compared to those predicted with an ANSYS finite element model. Additionally, the

experimental frequencies were compared with those measured with two conventional accelerometers bonded to the rail. The comparison between the video-based and the accelerometers-based frequencies showed excellent agreement demonstrating that the proposed non-contact approach can replace conventional accelerometers with the undoubtable advantage that the camera-based approach is truly non-contact, does not require specimen preparation, and does inform about the mode-shape being detected. In addition, every pixel of the image can be considered as a virtual accelerometer.

The comparison between the video-based and the ANSYS-based data revealed that the increase in compression made the rail stiffer, changing the effects of the boundary conditions on the frequencies of vibration. Owing to these outcomes, the finite element model was expanded and generalized in order to characterize the natural frequencies of vibration of a single rail under different lengths, boundary conditions, and axial stress.

Overall, the results presented in this article demonstrated that the proposed monitoring system is robust in terms of repeatability and sensitivity at detecting the vibration characteristics of rails. They also demonstrated that a reliable model of the rail under varying boundary conditions is necessary in order to link the modal characteristics to stress. In the future, the database of frequencies, mode-shapes, and axial stress created with the model can be used to train a machine learning algorithm to estimate the normal stress and therefore the neutral temperature of continuous welded rail using the equations presented in the Introduction.

Acknowledgements

The authors would like to acknowledge the sponsorship and support of the Federal Railroad Administration's Office of Research, Development and Technology under contract FR19RPD3100000022. The purchase of the high-speed camera was possible thanks to a small grant from AAR-TTCI University Program.

Compliance with Ethical Standards

Conflict of Interests

The authors declare that they have no conflict of interest.

References

[1] Kish, A., and G. Samavedam. 2005. "Improved destressing of continuous welded rail for better management of rail neutral temperature." Transp. Res. Rec. 1916 (1): 56–65. https://doi.org/10.1177/0361198105191600109.

[2] Product Marketing Sheet (2020) VERSE (Vertical Rail Stressing Equipment).

http://www.vortok.com/uploads/catalogerfiles/verse/Business_Case.pdf . Accessed 27 March 2020

[3] QinetiQ North America. Intelligent Rail Integrity System (IRIS).

https://www.qinetiq-na.com/wp-content/uploads/brochure_iris.pdf .

[4] Wegner A (2007) Prevention of track buckling and rail fracture by non-destructive testing of the neutral temperature in CW-rails. Proceedings International Heavy Haul Conference, Sweden, pp. 557-564

[5] Zhu X, Lanza di Scalea F (2016) Sensitivity to axial stress of electro-mechanical impedance measurements. Exp Mech 56(9): 1599-1610

[6] Phillips R, Lanza di Scalea F, Zhu X (2012) The influence of stress on Electro-mechanical impedance measurements in rail steel. Mater Eval 70(10): 1213-1218

[7] Hurlebaus S (2011) Determination of longitudinal stress in rails. Safety IDEA Project 15, Transportation Research Board, 01363276

[8] Nucera C, Lanza di Scalea F (2014) Nonlinear wave propagation in constrained solids subjected to thermal loads. J Sound Vib 333(2):541-554

[9] Nucera C, Lanza di Scalea F (2014) Nondestructive measurement of neutral temperature in continuous welded rails by nonlinear ultrasonic guided waves. J Acoust Soc Am 136(5):2561-2574

[10] Nucera C, Phillips R, Lanza di Scalea F, Fateh M, Carr G (2013) RAIL-NT System for the in-situ measurement of neutral temperature in CWR: results from laboratory and field test. J Transp Res Board, 01470560(13-3511), p 13

[11] Lanza di Scalea F, Nucera C, (2018) Nonlinear ultrasonic testing for non-destructive measurement of longitudinal thermal stresses in solids. US Patents, No. US20150377836A1

[12] Bagheri A, La Malfa Ribolla E, Rizzo P, Al-Nazer L, Giambanco G (2015) On the use of l-shaped granular chains for the assessment of thermal stress in slender structures. Exp Mech 55(3):543-558

[13] Bagheri A, La Malfa Ribolla E, Rizzo P, Al-Nazer L (2016) On the coupling dynamics between thermally stressed beams and granular chains. Arch of Appl Mech 86(3):541-556

[14] Bagheri A, Rizzo P, Al-Nazer L (2016) A numerical study on the optimization of a granular medium to infer the axial stress in slender structures. Mech Adv Mater Struct 23(10):1131-1143

[15] Nasrollahi A, Rizzo P (2018) Axial stress determination using highly nonlinear solitary waves. J Acoust Soc Am 144(4):2201-2212

[16] Nasrollahi A, Rizzo P (2019) Numerical analysis and experimental validation of an nondestructive evaluation method to measure stress in rails. ASME J Nondestruct Eval Diagn Progn Eng Syst (2019) 2(3):031002. https://doi.org/10.1115/1.4043949

[17] Feng D, Feng M Q (2016) Vision-based multipoint displacement measurement for structural health monitoring. Struct Control Health 23(5):876-890

[18] Ribeiro D, Calçada R, Ferreira J, Martins T (2014) Non-contact measurement of the dynamic displacement of railway bridges using an advanced video-based system. Eng Struct 75:164-180

[19] Feng D, Feng M Q (2017) Experimental validation of cost-effective vision-based structural health monitoring. Mech Syst Signal Process 88:199–211

[20] Chen J G, Wadhwa N, Cha Y J, Durand F, Freeman W T, Büyüköztürk O (2015) Modal identification of simple structures with high-speed video using motion magnification. J Sound Vib 345(9):58–71

[21] Wadhwa N, Rubinstein M, Durand F, Freeman W T (2013) Phase-based video motion processing. ACM Trans Graph 32(4):1-10

[22] Chen J G, Davis A, Wadhwa N, Durand F, Freeman W T, Büyüköztürk O (2017) Video camera–based vibration measurement for civil infrastructure applications. J Infrastruct Syst 23(3):B4016013

[23] Chen J G, Adams T M, Sun H, Bell E S, Büyüköztürk O (2018) Camera-based vibration measurement of the World War I memorial bridge in Portsmouth New Hampshire. J Struct Eng 144(11):04018207

[24] Sarrafi A, Zhu Mao C N, Poozesh P (2018) Vibration-based damage detection in wind turbine blades using phase-based motion estimation and motion magnification. J Sound Vib 421:300–318

[25] Sefa Orak M, Nasrollahi A, Ozturk T, Mas D, Ferrer B, Rizzo P (2018) Non-contact smartphone-based monitoring of thermally stressed structures. Sens J. http://dx.doi.org/10.3390/s1804125

[26] Wu H Y, Rubinstein M, Shih E, Guttag J, Durand F, Freeman W (2012) Eulerian Video Magnification for Revealing Subtle Changes in the World. ACM Trans Graph 31(4):1–8

[27] Simoncelli E P, Freeman W T (1995) The steerable pyramid: a flexible architecture for multi scale derivative computation, Proceedings of the1995 International Conference on Image Processing (ICIP 95), Vol.3, IEEE Comput Soc, Washington DC, pp 444–447

[28] Schmid, P. J. (2010). Dynamic mode decomposition of numerical and experimental data. Journal of fluid mechanics 656: 5-28.

[29] Tu, J. H., Rowley, C. W., Luchtenburg, D. M., Brunton, S. L., & Kutz, J. N. (2014). On dynamic mode decomposition: Theory and applications. Journal of Computational Dynamics 1(2): 391-421.

[30] Kerr A D (1978) Analysis of thermal track buckling in the lateral plane. Acta Mech 30(1-2):17-50.

[31] Donley M G, Kerr A D (1987) Thermal buckling of curved railroad tracks. Int J Non-Linear Mech, 22(3), pp. 175-192.

[32] Kerr A D (1978) Lateral buckling of railroad tracks due to constrained thermal expansions—a critical survey. Railr Track Mech Technol, Elsevier, pp 141-169

[33] Lim N H, Park N H, Kang Y J (2003) Stability of continuous welded rail track. Compu Struct 81(22-23):2219-2236

[34] Kerr A D (1980) An improved analysis for thermal track buckling. Int J Non-Linear Mech 15(2):99-114

[35] Kish A (2011) On the fundamentals of track lateral resistance. American Railway Engineering and Maintenance of Way Association (AREMA)

[36] Martínez I N, Sanchis I V, Fernández P M, Franco R I (2015) Analytical model for predicting the buckling load of continuous welded rail tracks. Proceedings of the Institution of Mechanical Engineers, Part F, J Rail Rapid Transit 229(5):542-552

[37] Lim N H, Park N H, Kang Y J (2003) Stability of continuous welded rail track. Comput Struct 81(22-23):2219–2236

[38] Kostovasilis D , Thompson D J, Hussein M F M (2017) A semi-analytical beam model for the vibration of railway tracks. J Sound Vib 393:321-337

[39] Livingston T, Beliveau J G, Huston D R (1995) Estimation of axial load in prismatic members using flexural vibrations. J Sound Vib 5:899–908

[40] Kish A, Samavedam G (2013) Track Buckling Prevention: Theory, Safety Concepts, and Applications. Final Report, DOT/ FRA/ORD-13/16

[41] Bayon A, Gascon F, Medina R, Nieves F J, Salazar F J (2012) On the flexural vibration of cylinders under axial loads: Numerical and experimental stusty. J Sound Vib 331:2315–2333

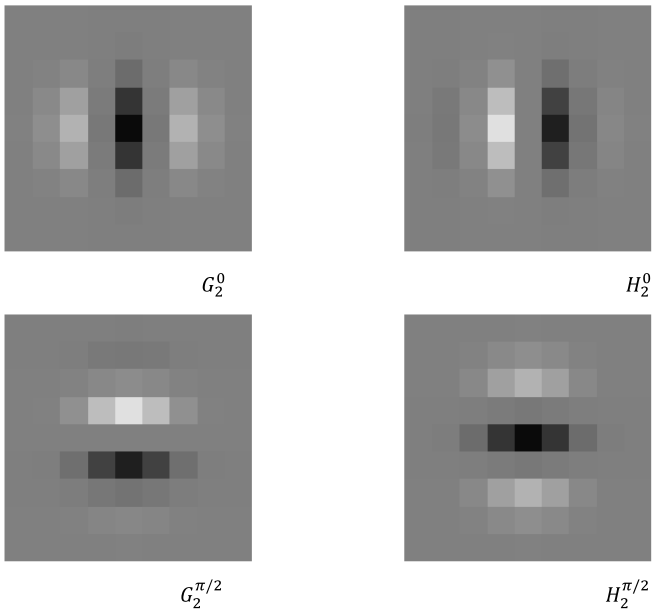

Figure 1 Filters used in the image processing study to compute local phase and local amplitude [21]

Figure 2 Schematics of the rail and its boundary conditions. Rotational and torsional springs were used to mimic the restraints along the three axis. The lateral direction indicate flexural bending along the weak axis of inertia whereas the transverse direction identifies the bending along the strong axis of inertia

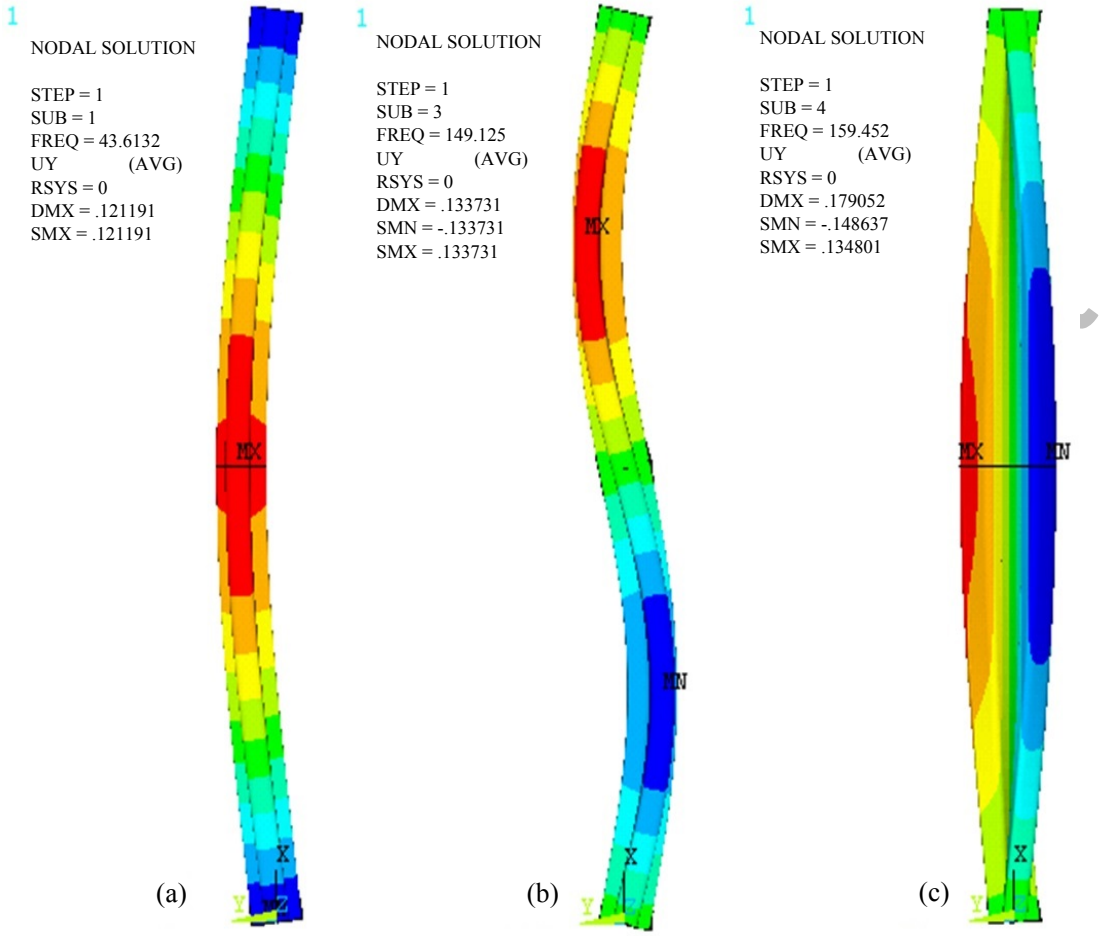

Figure 3 Numerical model results associated with a 2.4 m long AREMA 132, whose torsion is fully restrained at both ends and the flexural spring coefficients are equal to *1.8EI/L*. Lowest flexural **a**, coupled flexural-torsional **b**, and torsional mode shape **c**

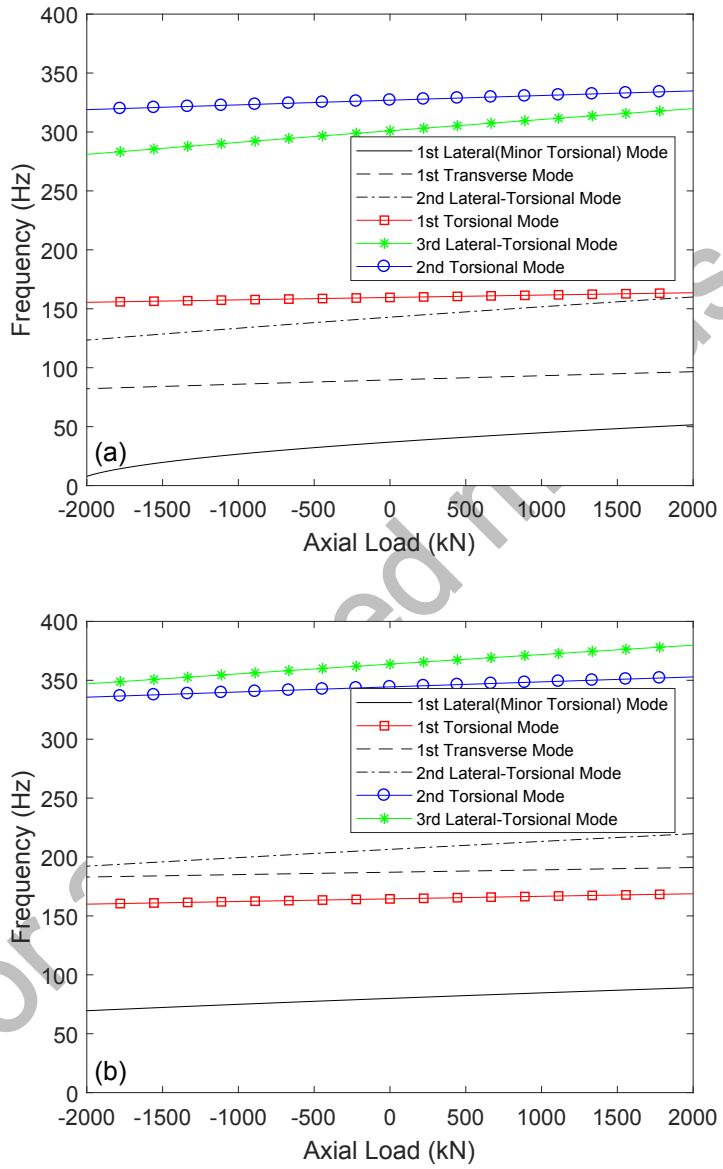

Figure 4 Numerical model results associated with a 2.4 m long AREMA 132 fully restrained to torsion at both ends. Frequency as a function of axial load for a pinned-pinned **a** and fixed-fixed **b** rail

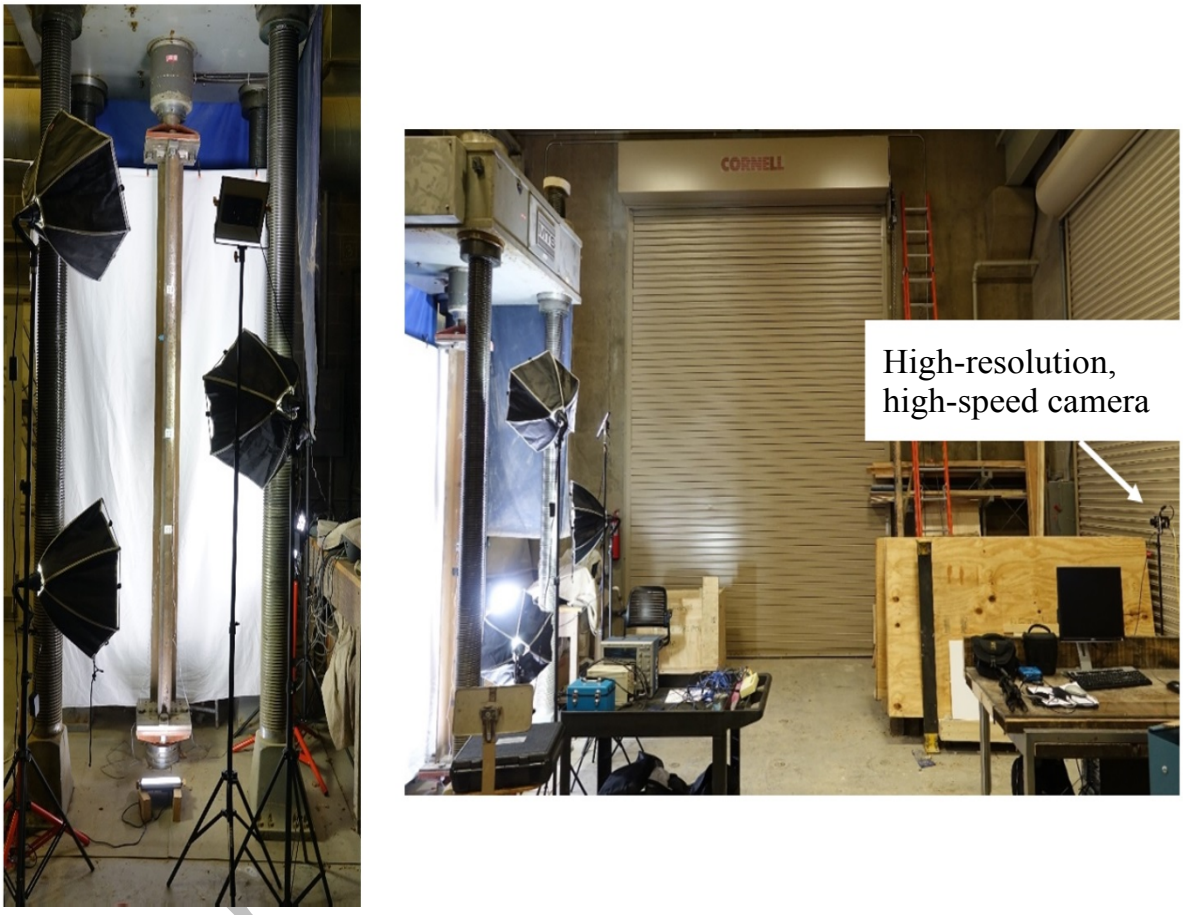

Figure 5 Photos of the experimental setup

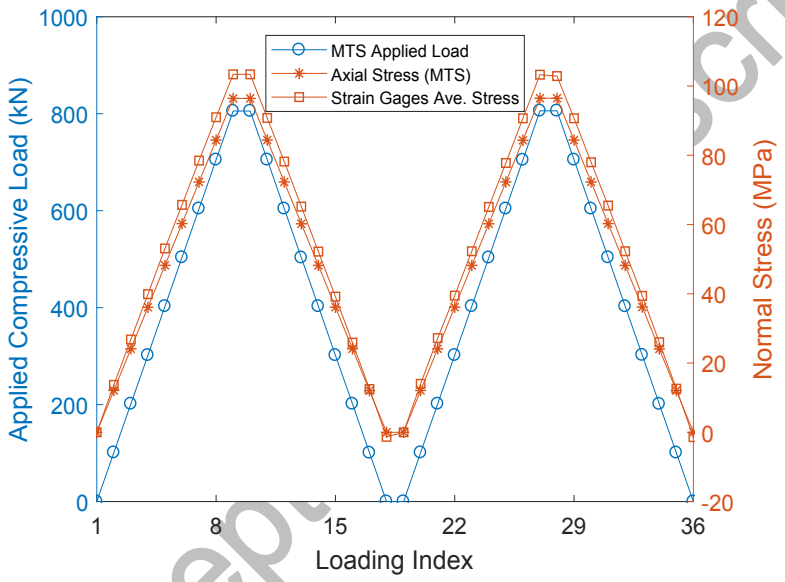

Figure 6 Experimental results. Compressive load and corresponding stress measured with the MTS machine and two strain gages mounted on the specimen, respectively. The loading index indicates the measurement steps taken during the experiment. Index = 1 indicates the first measurement taken during the first compression loading ramp at zero force. To ease visualization, the load and the stress curves are offset slightly

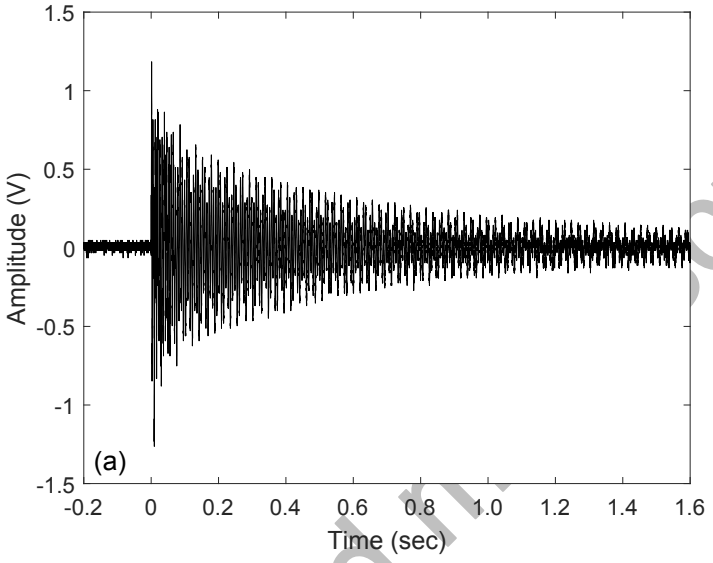

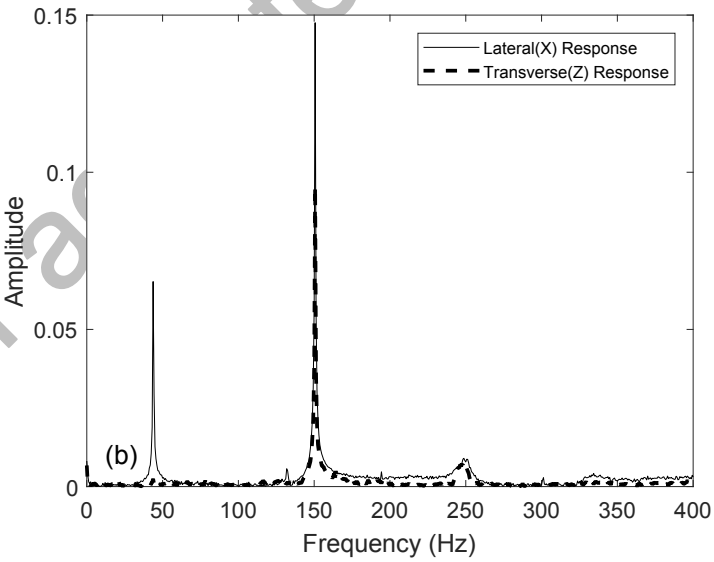

Figure 7 Experimental results. **a** Time-series recorded by one of the accelerometers under 805 kN compression along the lateral direction. **b** Corresponding Fourier Transform overlapped to the Fourier Transform of the transverse direction

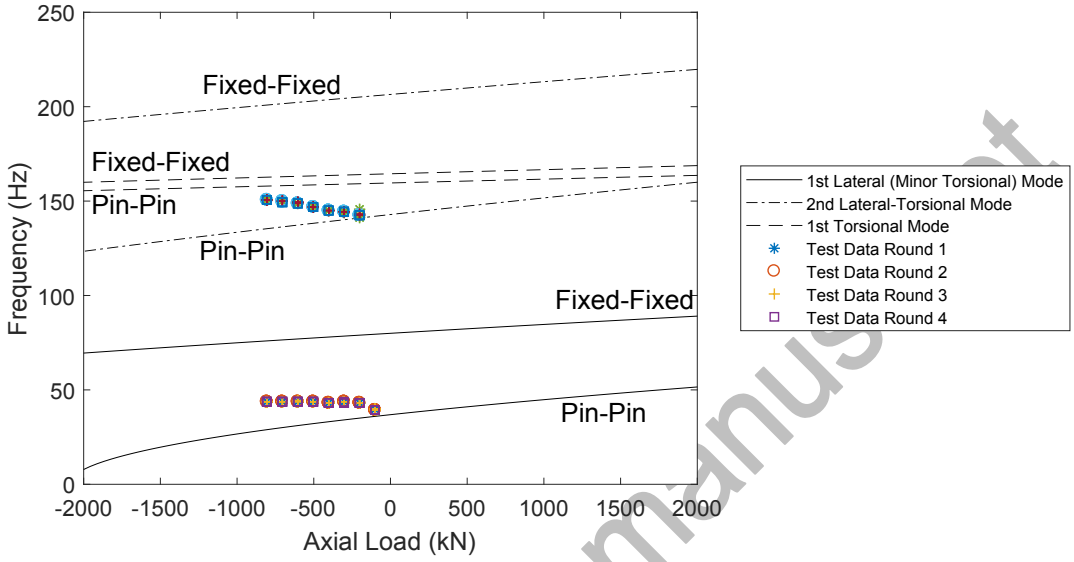

Figure 8 Numerical predictions of the natural frequencies as a function of axial load for the rail specimens. The experimental frequencies are overlapped for direct comparison

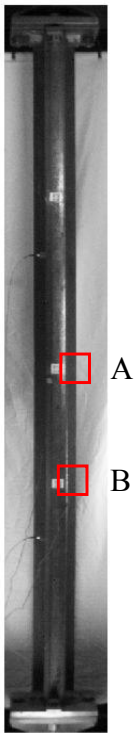

Figure 9 Video processing. Example of unprocessed video frame recorded during the experiment. The boxes **a** and **b** indicate the edges at the two "QR" sheets attached to the rail to enhance contrast

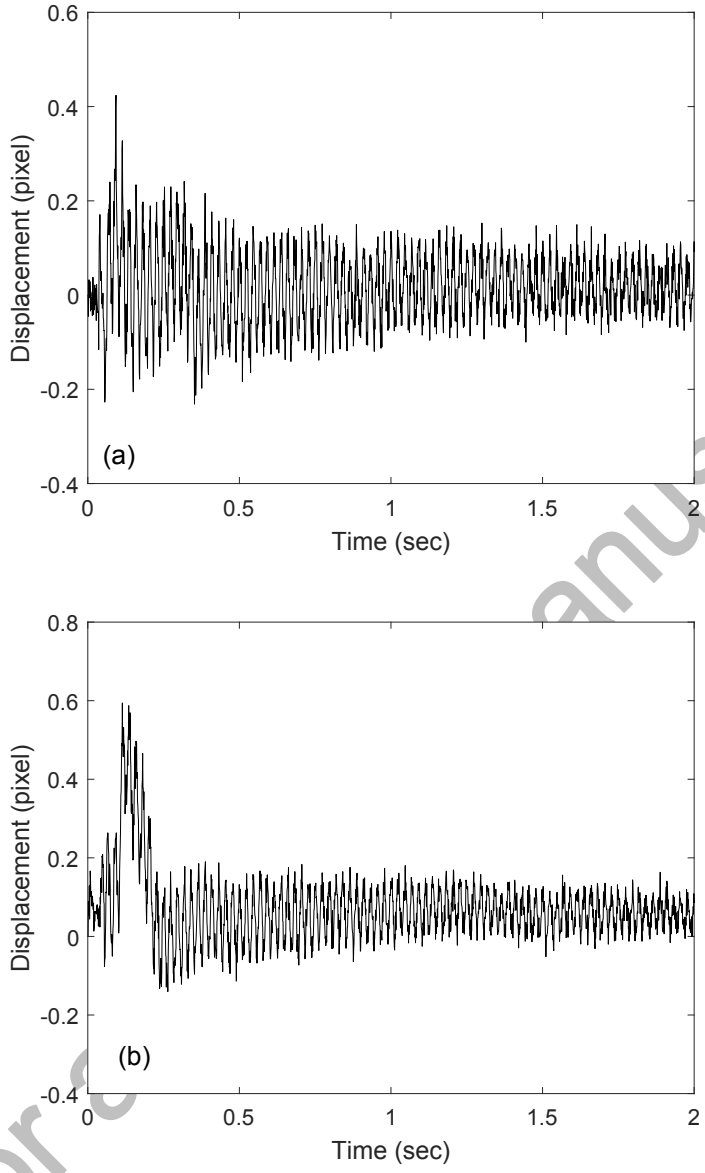

Figure 10 Video processing. Example of time history displacement extracted from boxes point A **a** and B **b** using video processing

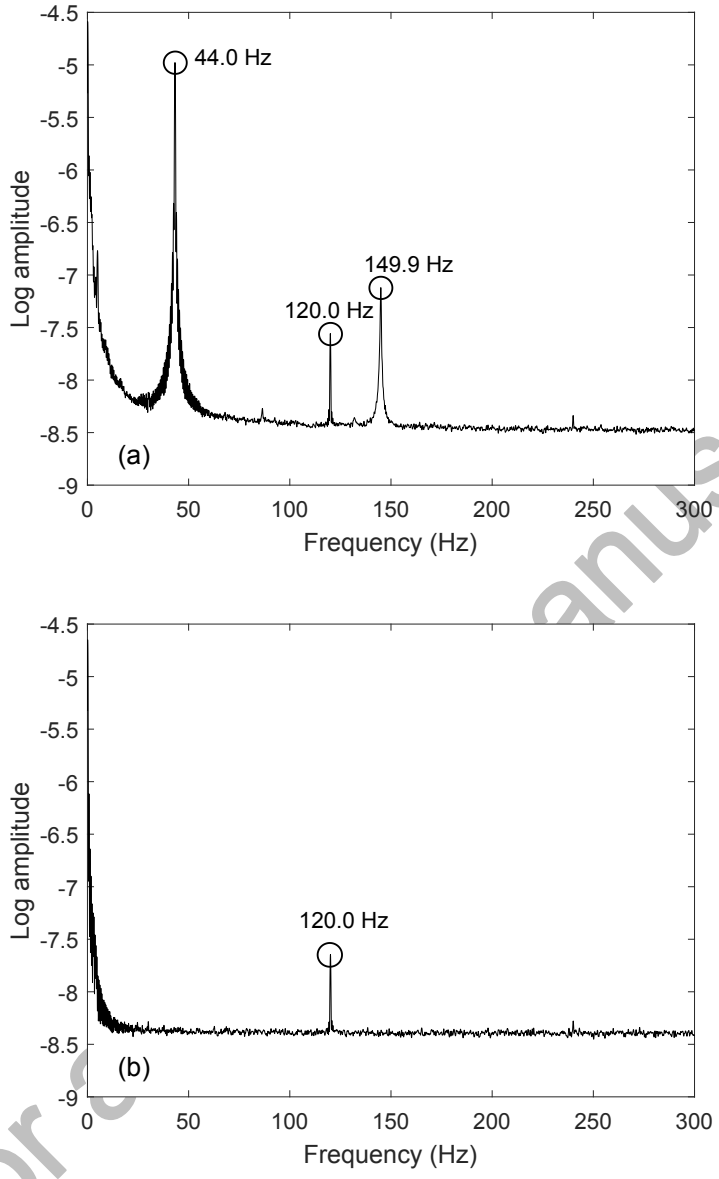

Figure 11 Video processing. Example of Fast Fourier Transforms extracted from the displacements time series during the experiment

Figure 12 Video processing. Snapshot of the magnified videos with frequency peak 1 **a** and 3 **b**. For the peak 1, the magnification frequency band is 42Hz-46Hz and amplification factor 100. For the peak 3, the magnification frequency band is 148Hz-152Hz and amplification factor 300

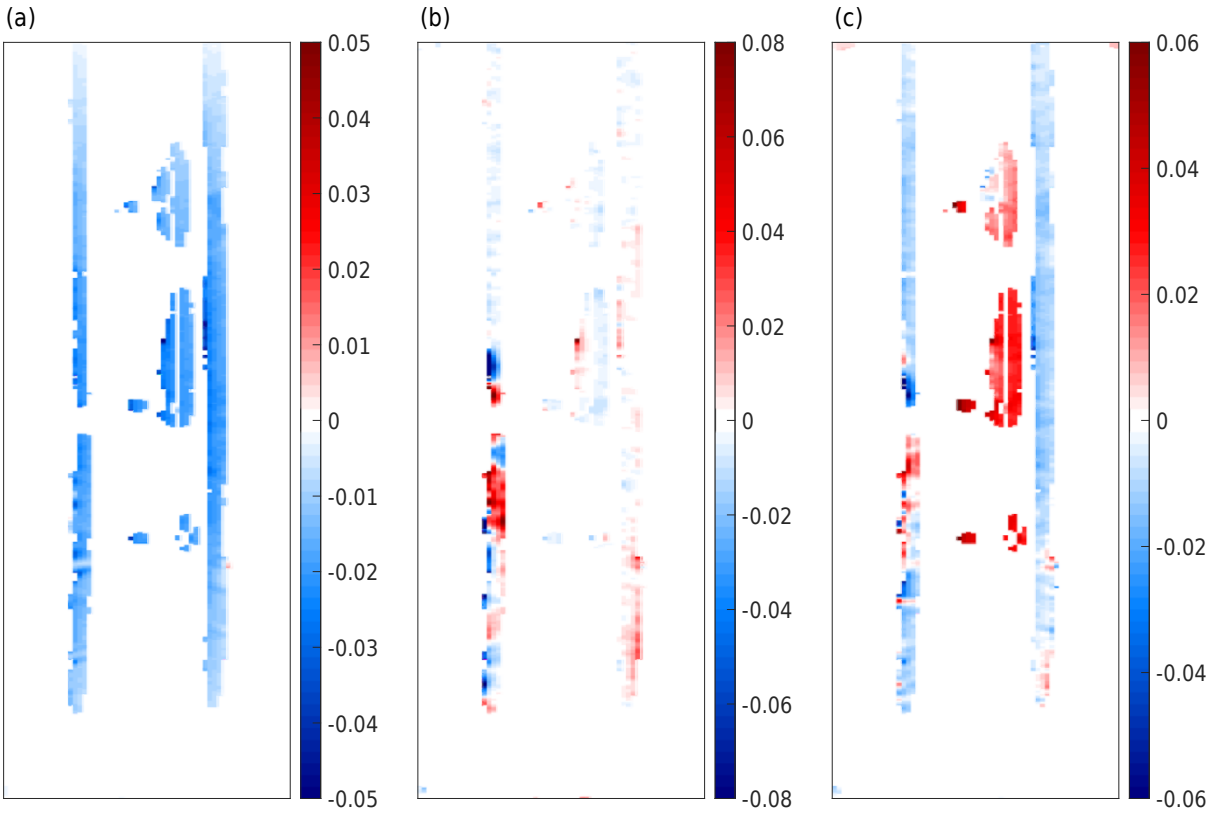

Figure 13 Video processing. Decoupled mode shapes from dynamic mode decomposition (DMD). **a** shows the first lateral vibration mode for the frequency peak 44.0 Hz in Fig. 12. While **c** represents the torsion mode for the frequency peak 149.9 Hz in Fig. 12. **b** represents the fake mode induced by the light noise

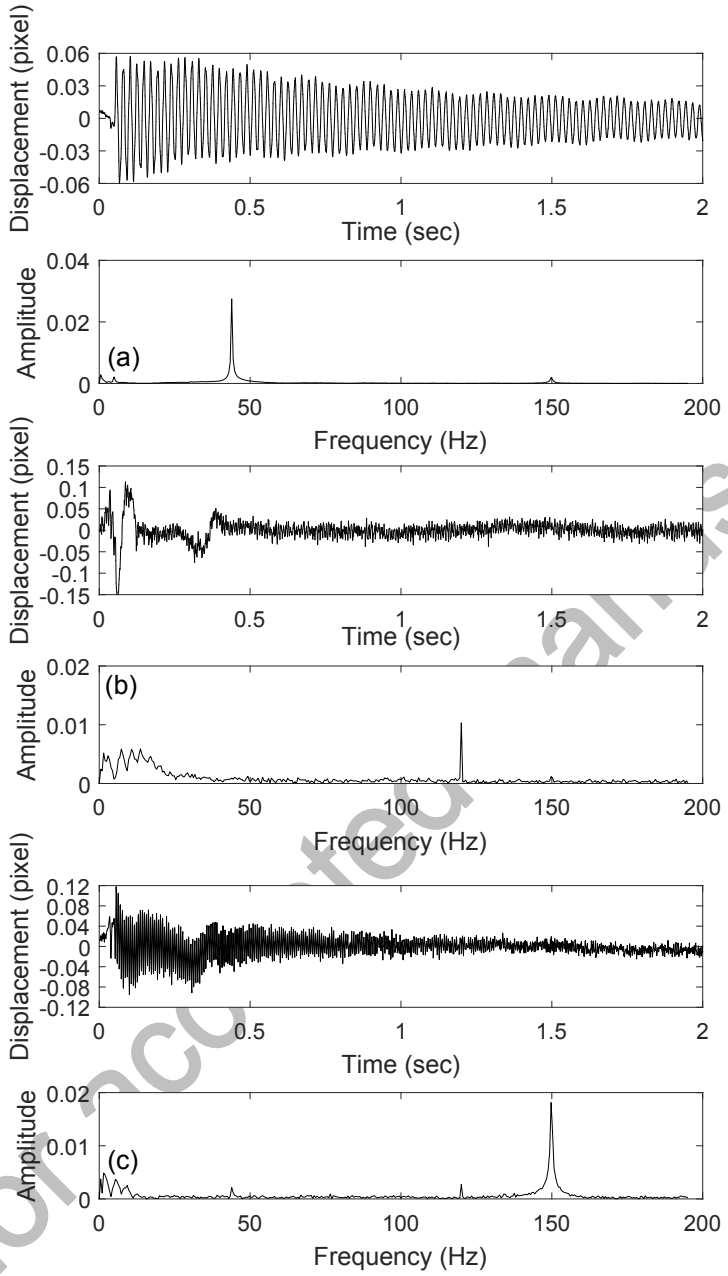

Figure 14 Video processing. Source signals and their frequency spectrums of the mode shapes from DMD. **a**, **b** and **c** respectively represents the source signal of the mode shape **a**, **b** and **c** shown in Fig. 14

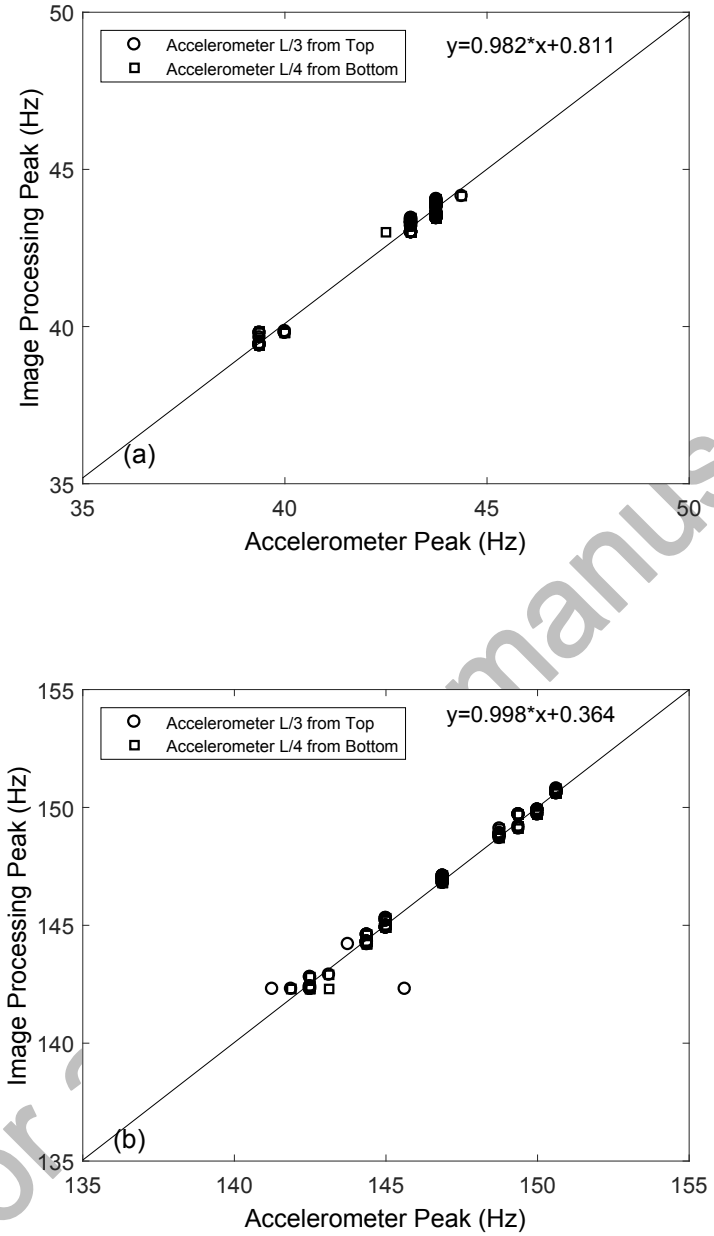

Figure 15 Peak frequencies obtained by image processing versus peak frequencies by accelerometers for peak 1 **a** and 3 **b**. Each dot corresponds to a single loading condition during two complete cycles of load and unloading

Table 1 – Variable parameters along with considered values in the FE modeling of the rail

Parameter	***Minimum value***	***Maximum value***	***No. of increments for the given parameter***
Length	*0.5 meters*	*4 meters*	*15*
Axial Load	*70% compression (with respect to pin-pin buckling)*	*20% tension*	*37*
Flexural Spring Coefficient	*0 (pin-pin case)*	*60 EI/L*	*17*
Torsional Spring Coefficient	*10 GJ/L*	*100 GJ/L*	*3*